PHYSICAL REVIEW FLUIDS **2**, 093301 (2017)

Shear-induced ordering and crystallization of jammed suspensions of soft particles glasses

Fardin Khabaz,[1] Tianfei Liu,[1] Michel Cloitre,[2] and Roger T. Bonnecaze[1,*]
[1] *McKetta Department of Chemical Engineering, The University of Texas at Austin, Austin, Texas, 78712, USA*
[2] *Soft Matter and Chemistry, CNRS, ESPCI Paris, PSL Research University, 10 Rue Vauquelin, 75005 Paris, France*

(Received 18 May 2017; published 1 September 2017)

The microstructure and shear rheology of highly concentrated, jammed suspensions of soft particles are shown to depend on polydispersity and shear rate from computational simulations. Rich behavior is observed depending on the degree of polydispersity and the shear rate. Glassy suspensions with a low degree of polydispersity evolve to face-centered cubic and hexagonal close-packed structures at low and high shear rates, respectively. The structural rearrangement occurs over several units of strain and reduces the shear stress and elastic energy. Suspensions with a higher degree of polydispersity exhibit a microstructural transition from a glass to a layeredlike structure for sufficiently high shear rates. In this case, the soft particles first rearrange themselves in the flow-vorticity plane during an induction time (or strain) before layers parallel to the flow-vorticity plane are formed. The induction strain decays exponentially with shear rate revealing that the devitrification of monodisperse and polydisperse suspensions is a shear-activated process. Finally, a generic dynamical state diagram is found that depends on the polydispersity and the ratio of viscous to elastic forces due to shear.

DOI: 10.1103/PhysRevFluids.2.093301

I. INTRODUCTION

The macroscopic properties of colloidal dispersions are determined by the spatial arrangement of the particles into the microstructure. In the quiescent state, many different structures are found depending on the relative importance of the Brownian, repulsive, and attractive forces. Monodisperse Brownian hard spheres [1,2], which interact only through repulsive excluded volume interactions, exhibit a liquid phase at low volume fractions beneath $\phi = 0.494$, where they start crystallizing. Liquid-crystal coexistence is observed at volume fractions between 0.494 and 0.545; a fully crystalline state consisting of a mixture of hexagonally close-packed (HCP) and face-centered-cubic (FCC) domains exists between 0.545 and 0.58. Above $\phi = 0.58$, particles are trapped in an arrested glass phase. Polydispersity is known to obviate crystallization [3–7]; the suspension then stays in a supercooled state up until it forms a glass at $\phi = 0.58$. Barrat and Hansen [3] used density functional theory and showed that the required polydispersity to inhibit the crystallization (i.e., terminal polydispersity) for hard spheres is in the range of 0.06–0.07. Monte Carlo simulations predicted a value of 0.057 for the terminal polydispersity of hard sphere [4,5]. Pusey [6] showed that in experiments the terminal polydispersity is in the range of 0.06 to 0.12.

The state diagram of soft repulsive microgels exhibits apparent similarities with that of hard-sphere suspensions. For instance, microgel suspensions have been found to undergo the same sequence of transitions from fluid to crystal to amorphous solid with increasing volume fraction [8–12]. Suspensions of soft sphere polymer micelles also undergo a transition from fluid to crystal states with increasing volume fraction [13]. However several major quantitative differences signal the role of softness [14]. First, the onset of crystallization and the extent of the phase coexistence region depend on the degree of softness [8,13,15]. For instance, crystallization is strongly inhibited in hairy

---

[*] rtb@che.utexas.edu

suspensions like star polymers because the dangling chains can locally interpenetrate and fluctuate beyond the limit allowed by the Lindeman criterion [16]. Second, particles can be compressed well above close-packing where they come into contact and form a disordered jammed state [17]. In this regime, Brownian motion is negligible compared to the elastic energy associated with deformation at contact. Again the role of polydispersity is to suppress crystallization so that only three regimes are usually observed in polydisperse soft particle suspensions: liquid suspension, entropic glass, and jammed glass [18].

The application of oscillatory or steady shear flows is known to affect the microstructure of colloidal suspensions and the rheology [19]. The case of model hard-sphere suspensions made of sterically stabilized colloidal particles has attracted a lot of attention. Two decades of experiments have revealed a rich phenomenology [20–28]. When subject to oscillatory shear, hard-sphere suspensions exhibit various structures: FCC crystals, stacked layers with HCP symmetry, string and liquidlike structures, and tilted layers [21,29]. The exact morphology depends on a number of parameters, such as the volume fraction, the amplitude, and frequency of the solicitation and the shearing history. Suspensions with a fluidlike ordering at equilibrium or glasses tend to crystallize under oscillatory shear [20,21,24,26,29]. Three-dimensional crystals at equilibrium are transformed into two-dimensional structures [21,24]. These shear-induced structures vanish upon flow cessation. Generally, FCC ordering appears at low strain and frequency amplitude and hexagonally close-packed layer at higher amplitudes. Out-of-equilibrium phase diagram has been proposed to rationalize the structural changes occurring upon shearing [21,29]. In a study by Koumakis *et al.* [30], the elastic and viscous moduli of suspension composed of PMMA particles with a volume fractions close to the random close packing were significantly smaller than their glass counterparts. Furthermore, the obtained crystals in the experiments were not in a thermodynamic equilibrium. Similar trends are observed in steady continuous flow and Poiseuille flow [23,25,27]. On the numerical side Butler and Harrowell used Brownian dynamics simulations and showed that below the melting temperature, suspension turns into hexagonal packed strings which are aligned in the flow direction, while above the melting temperature, it forms unstructured layers in the shear plane [31].

Charge stabilized hard-sphere suspensions constitute another class of suspensions that has been intensively studied [32–43]. Particles interact through a long-ranged repulsive potential which promotes crystallization at equilibrium. Shear-induced structures consisting of stacks of two-dimensional crystal-layers with hexagonal symmetry are generally reported. Several papers describe the transformation of the equilibrium crystal in relation to the rheological properties of the suspensions [32,34,37,42]. When subjected to increasing shear rate, the equilibrium structure exhibit two reversible transitions: (i) at low shear rates, the 3D crystals transforms into sliding two-dimensional HCP layers; (ii) at higher shear rates, the layers melt into an amorphous structure [32,34,38,42]. Melting induced by shear has been reported by several authors [36].

Although soft particles are also prone to crystallize, the effect of shear on soft particles glasses and crystals has been scarcely examined. The role of shear seems to depend on the intensity. Upon the application of a small shear, the polycrystalline phase of a block copolymer abruptly transforms into a single crystal [44]. One very comprehensive study concerns the ordering of poly(methyl methacrylate) (PMMA) microgel suspensions subjected to oscillatory shear [9]. Different phases are reported depending on the initial volume fraction and the strain amplitude. When the volume fraction is below $\phi = 0.548$, i.e., the volume fraction at which hard spheres crystallize, oscillatory shear never induces ordering. Above $\phi = 0.548$, crystalline order with FCC symmetry is obtained at low strain amplitude, random-stacked structures consisting of planes of HCP particles aligned parallel to the flow-vorticity plane at larger amplitude, and finally stringlike structures resulting from the breaking the random-stacked structure at high strain amplitudes. A glass-to-crystal transition was also found in star polymer solutions [45] with a similar sequence of structural transitions [46]. Two-dimensional stacked HCP layers of particles have also been observed in PNIPAm microgels [47], polymeric micelles [48–50], and cluster crystals [51]. A few generic features, among which the prominence of the HCP sliding layer structure at relatively high shear rates sometimes followed by melting,

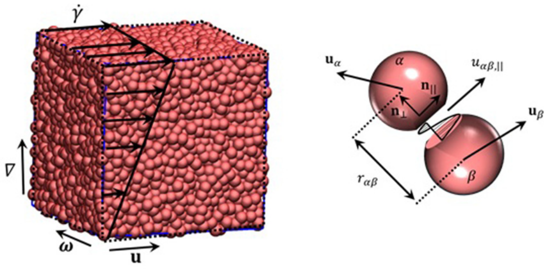

(a) (b)

FIG. 1. (a) Configuration of a suspension with a volume fraction of 0.9 and polydispersity index of $\delta = 0.1$ that is in shear flow with an applied shear rate of $\dot{\gamma}$. The flow (**u**), gradient (∇), and vorticity ($\boldsymbol{\omega}$) directions are shown in the figure. (b) Schematic showing pair-wise interaction between particles α and β.

emerge from this critical analysis of the literature. However, many important questions remain open. First, since polydisperse suspensions never crystallize under shear, it is clear that a complete out-of-equilibrium state diagram must include the degree of polydispersity of the suspensions in addition to the flow parameters and the volume fraction. It is likely that this would help to rationalize the diversity of observations made in experiments where the polydispersity index is rarely specified. Second, the question of the physical mechanisms leading to shear ordering from initially disordered suspensions is not addressed with only a few exceptions [27,38,41]. Third, the connection between structure and rheology in concentrated suspensions remains an important issue especially in highly concentrated suspensions [28].

In this paper we address these issues for the case of jammed suspensions of soft spherical particles. We capitalize on a micromechanical model initially developed for describing the rheology of soft particle glasses under steady and oscillatory shear deformation [52,53]. We consider three-dimensional suspensions of elastic particles packed at volume fractions well above the jamming transition that interact through a nonlinear Hertzian pair-wise interaction. This model has been shown to quantitatively describe the linear and nonlinear rheology of a wide range of materials such as emulsions and microgels. Here we investigate the structural changes induced by the application of a steady shear flow to jammed suspensions prepared in the amorphous state, starting from monodisperse particle distributions and subsequently increasing the polydispersity. We show that monodisperse jammed glassy suspensions devitrify and become ordered upon flow inception. FCC crystals form at low shear rates and reversibly transform at larger shear rates into sliding layers. Polydispersed suspensions exhibit a transformation from the amorphous state to sliding HCP layers at a sufficiently shear rate after an induction time. In both cases the sliding layers are parallel to the flow-vorticity plane. The arrangement of particles in the flow-gradient plane is well described by a HCP morphology. The layered state is metastable and disappears when the shear rate is decreased or suppressed. We demonstrate that this disorder-layering transformation is a shear-activated process associated with a specific rearrangement of particles in the flow-vorticity plane. A model quantitatively accounts for the variation of the induction time with the applied shear rate when the volume fraction and the polydispersity index are varied.

II. SIMULATION METHOD

We model soft particle glasses as a suspensions of N non-Brownian elastic particles in a solvent with a viscosity of η_s which are jammed in a cubic simulation box at volume fractions larger than the random close-packing of hard spheres, as shown in Fig. 1(a) [52,54]. Suspensions with volume fractions of $\phi = 0.7$,0.8, and 0.9 were studied. Gaussian size distributions with standard deviation values of zero for monodisperse and values of $\delta = 0.02$, 0.05, 0.1, and 0.2 were used to make the suspensions polydisperse, where the average radius of the particles is unity; δ is termed the polydispersity index in the following. The particles were initially placed in a cubic box and the box size was reduced using Lubachevsky and Stillinger compression algorithm [55]. After reaching the close-packed structure, the spheres were assumed deformable, and the box size was reduced further in small steps. At contact, particles α and β create a flat facet resulting in a deformation of $\varepsilon_{\alpha,\beta} = 0.5(R_\alpha + R_\beta - r_{\alpha\beta})/R_c$, where R_α and R_β are the radii of particles α and β, $r_{\alpha\beta}$ is the center-to-center distance, and R_c is the contact radius, which is given as $R_c = R_\alpha R_\beta/(R_\alpha + R_\beta)$. At this point the particles are not in force equilibrium. The positions of the particles can be relaxed to ensure the particles are in force equilibrium and minimize the energy of the system [56]. However, the steady-state rheology and structures observed do not depend on the initial conditions of the suspensions.

The model proposed by Seth *et al.* [52] considers both elastic repulsion and elastohydrodynamic (EHD) forces between particles, as shown in Fig. 1(b). The elastic repulsion force between particles α and β is given by the generalized Hertz law:

$$\mathbf{f}^{e}_{\alpha\beta} = \tfrac{4}{3} C E^{*} \varepsilon^{n}_{\alpha\beta} R_c^2 \mathbf{n}_{\perp}, \tag{1}$$

where E^* is the particle contact modulus ($E^* = E/2(1-\nu^2)$, with E being the Young modulus, $\nu = 0.5$ is the Poisson ratio). C and n are parameters that depend on the degree of compression. For $\varepsilon < 0.1$, $n = 1.5$ and $C = 1$, for $0.1 \leqslant \varepsilon < 0.2$, $n = 3$ and $C = 32$, and if $0.2 \leqslant \varepsilon < 0.6$, then $n = 5$ and $C = 790$ [52,57]. $\mathbf{n}_\perp$ is the perpendicular direction to the facet at contact. The EHD drag force, which is due to the existence of thin film of solvent between the flat facets of two particles in contact during the shear deformation, is given by

$$\mathbf{f}^{\mathrm{EHD}}_{\alpha\beta} = -\left(\eta_s C u_{\alpha\beta,||} E^{*} R_c^3\right)^{1/2} \varepsilon_{\alpha\beta}^{(2n+1)/4} \mathbf{n}_{||}, \tag{2}$$

where $u_{\alpha\beta,||}$ is relative velocity component in the direction of $\mathbf{n}_{||}$, which is direction parallel to the facet at contact. These two forces were assumed to be pairwise additive, and the fluid inertia was neglected [52,53]. The velocity field due to the motion of the solvent is given as $\mathbf{u}^{\infty}_{\alpha} = \frac{\dot{\gamma}\eta_s}{E^*} y \mathbf{e}_x$, where $\mathbf{e}_{\mathrm{x}}$ is the basis vector in the x direction. The dimensionless equation of motion (length, time, and velocity are nondimensionalized by R, η_s/E^*, and RE^*/η_s, respectively) for each particle can be written as

$$\frac{d\mathbf{x}_\alpha}{dt} = \mathbf{u}^{\infty}_{\alpha} + \frac{f_r(\varphi)}{6\pi R_\alpha}\left[\frac{4}{3} C \sum_{\beta} \varepsilon^{n}_{\alpha\beta} R_c^2 \mathbf{n}_{\perp} - \sum_{\beta} \left(C u_{\alpha\beta,||} R_c^3\right)^{1/2} \varepsilon_{\alpha\beta}^{(2n+1)/4} \mathbf{n}_{||}\right], \tag{3}$$

where $\mathbf{x}_\alpha$ is the position of the particle α and $f_r(\varphi)$ is the mobility function, which was set to 0.01 in the simulations [52,53].

Systems with $N = 10^3$ particles were prepared to characterize the response of jammed suspensions under steady shear deformation. The Lees-Edwards [58] boundary conditions were utilized in the LAMMPS package [59] to impart the desired shear rate to the simulation box. A wide range of shear rate ($\tilde{\dot{\gamma}} = 10^{-9} - 10^{-3}$, where $\tilde{\dot{\gamma}}$ is the nondimensional shear rate given by $\tilde{\dot{\gamma}} = \frac{\dot{\gamma}\eta_s}{E^*}$) was employed to determine the shear stress of the systems. The stress tensor was calculated using the Kirkwood formula [60]: $\sigma = \frac{1}{V}\sum_{\beta}^{N}\sum_{\alpha>\beta}^{N} \mathbf{f}_{\alpha\beta}(\mathbf{x}_\alpha - \mathbf{x}_\beta)$, where V is the volume of the system and $\mathbf{f}_{\alpha\beta}$ is the total force acting on particle α from particle β. The elastic energy was determined by integrating the force acting on particles: $U = \frac{8}{3(n+1)}\sum_{\alpha=1}^{N}\sum_{\beta>\alpha}^{N} C E^{*} \varepsilon_{\alpha\beta}^{n+1} R_c^3$, where C and n parameters are as the same as those used in the force law in Eq. (1). The simulations were performed for 100 strain units and the stress tensor was calculated at regular intervals. Although the simulation results were insensitive to the value of the time step below value of 10^{-2} for a nondimensional shear rate of 10^{-4}, it was chosen such that it produced 10^7 steps per strain at each shear rate. We note that results for the shear rheology presented here are the same for simulations with 125, 10^3, and 10^4 particles.

Structural properties of the system were characterized by determining the pair distribution function in suspensions with $N = 10^4$ particles. The pair distribution functions $g_{u\nabla}(\rho)$ and $g_{u\omega}(\rho)$ in the flow-gradient and flow-vorticity planes were computed at different strain values to investigate the structural rearrangement as a function of the simulation time. Here, ρ is the magnitude of the two-dimensional position vector of a given particle in the flow-gradient and flow-vorticity planes that is normalized by the radius of the particle.

To connect the microstructure to macroscopic properties of suspensions, the dynamic pair distribution function between the particles were determined by decomposing it into an orthogonal series of spherical harmonic functions [61],

$$g(\mathbf{r}) = g_s(r) + \sum_{l=1}^{\infty} \sum_{m=-l}^{l} g_{lm}(r) Y_{lm}(\theta,\phi). \tag{4}$$

The coefficient $g_{2,-2}(r)$ of the expansion of $g(\mathbf{r})$ can be used to determine the shear stress,

$$\sigma_{yx} = -n^2 \sqrt{\frac{\pi}{15}} \int_0^{2R} r^3 f^e(r) g_{2,-2}(r) dr, \tag{5}$$

where n is the number density of particles and $f^e(r)$ is the elastic contribution of the force.

We also used bond order parameters to characterize the crystal structure of the monodisperse systems studied [15]. A bond is defined as a connection between particles i and j that are within a cutoff distance, which here is assumed to be 2.20. The local bond order parameter Q_{lm} is defined as

$$Q_{lm}(\mathbf{r}) \equiv Y_{lm}(\theta(\mathbf{r}),\phi(\mathbf{r})), \tag{6}$$

where $\mathbf{r}$ is the bond between the neighboring particles, $\theta(\mathbf{r})$ and $\phi(\mathbf{r})$ are the polar and azimuthal angles, respectively, and Y_{lm} are the spherical harmonics. The average bond order can be determined by averaging the local bond order parameters over the number of bonds (N_b) in the system:

$$\bar{Q}_{lm} \equiv \frac{1}{N_b} \sum_{\text{bonds}} Q_{lm}(\mathbf{r}). \tag{7}$$

To eliminate the dependence of bond order parameters on the rotation of the frame of reference, we calculate the second-order (Q_l) and third-order (W_l) invariants as follows:

$$Q_l \equiv \sqrt{\frac{4\pi}{2l+1} \sum_{m=-l}^{l} |\bar{Q}_{lm}|^2}, \tag{8a}$$

$$W_l \equiv \sum_{\substack{m_1,m_2,m_3 \\ m_1+m_2+m_3=0}} \begin{pmatrix} l & l & l \\ m_1 & m_2 & m_3 \end{pmatrix} \bar{Q}_{lm_1} \bar{Q}_{lm_2} \bar{Q}_{lm_3}, \tag{8b}$$

where $\left(\begin{smallmatrix} l & l & l \\ m_1 & m_2 & m_3 \end{smallmatrix}\right)$ are the Wigner $3j$ symbols [15]. It is also suggested to normalize the W_l values with respect to Q_{lm} as follows [15]:

$$\hat{W}_l \equiv \frac{W_l}{\left(\sum_m |Q_{lm}|^2\right)^{3/2}}. \tag{9}$$

The values of the bond order parameters (Q_l and $\hat{W}_l$) for an amorphous liquid are zero, and they are nonzero for even values of l when the structure has some degrees of crystallinity. We use four bond order parameters to determine the crystal structure, namely, Q_4, Q_6, $\hat{W}_4$, and $\hat{W}_6$ [62]. These provide a quantitative metric to determine whether a crystalline structure for monodispersed suspensions is HCP or FCC.

III. RESULTS AND DISCUSSION

A. Shear stress and elastic energy

The effects of polydispersity and volume fraction on shear stress and elastic energy per unit volume of suspension as functions of strain at a nondimensional shear rate of $\tilde{\dot{\gamma}} = \frac{\dot{\gamma}\eta_s}{E^*} = 10^{-4}$ are

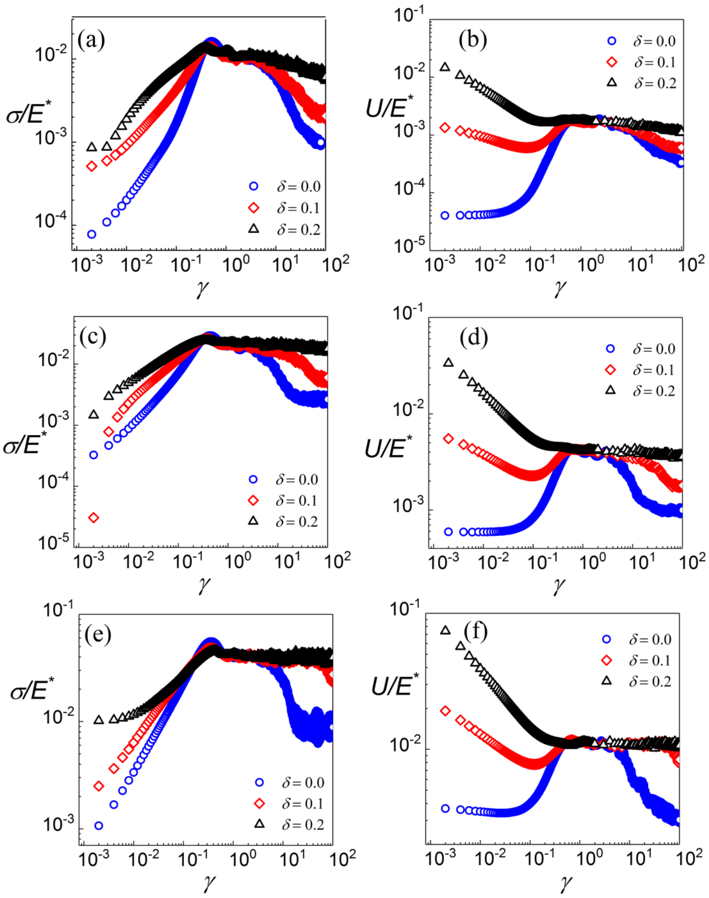

FIG. 2. Shear stress (left panel) and elastic energy (right panel) as a function of strain for different values of the polydispersity index and (a, b) $\phi = 0.7$, (c, d) $\phi = 0.8$, and (e, f) $\phi = 0.9$. The applied shear rate is $\tilde{\dot{\gamma}} = 10^{-4}$.

shown in Fig. 2. At a low volume fraction of 0.7 [Fig. 2(a)], the shear stress initially increases (linear elastic behavior) and shows a maximum value at a strain $\gamma \sim 0.1 - 0.3$, which is in the range of a typical yield strain of these materials. At this point the shear stress plateaus for several strain units, then decreases and reaches a steady-state value. The stress value at the plateau is the same regardless of the polydispersity.

For the suspensions with a low polydispersity index, there is an induction strain before a rapid drop in the shear stress to its steady-state value. This drop in the shear stress occurs at a slower rate for suspensions with a larger polydispersity index. The elastic energy behaves in a similar manner as seen in Fig. 2(b).

For suspensions with greater polydispersity, the elastic energy initially decreases, and depending on the degree of the polydispersity, it shows either a plateau region or maximum value, and then it reduces to a final steady-state value. The initial decrease in the elastic energy of the polydisperse suspensions is due to the existence of large overlaps between the polydisperse particles at the beginning of the shear simulations. These initial overlaps do not affect the final states of the polydisperse suspensions subjected to shear flow. At a higher volume fraction of 0.9 [Figs. 2(c) and 2(e)], the shear stress shows a very long plateau region as a function of the strain. This plateau persists during the entire simulation for the suspension with polydispersity index of 0.2. The elastic energy shows the same trend as seen in Figs. 2(d) and 2(f).

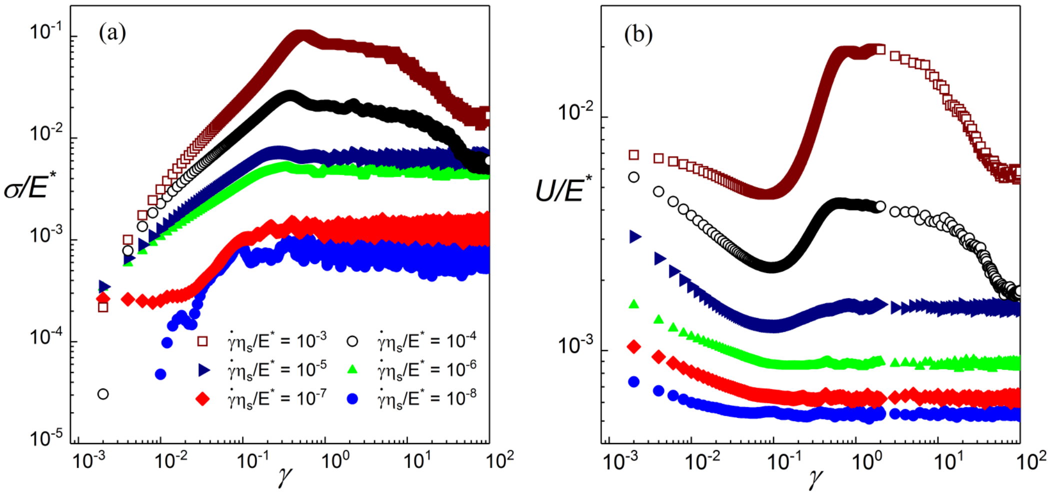

FIG. 3. (a) Shear stress and (b) elastic energy as a function of strain at different shear rates for a suspension with $\delta = 0.1$ and $\phi = 0.8$. The symbols in (b) are at the same shear rate as (a).

For a given volume fraction, the length of the induction strain plateau increases with increasing polydispersity. The induction strain is around seven for monodisperse suspensions [Figs. 2(c) and 2(d)]. When the polydispersity index is 0.20, the shear stress and elastic energy immediately reach their steady-state values. The induction strain is the same for both the elastic energy and shear stress. In addition as the volume fraction increases at a constant degree of polydispersity, the shear stress increases as expected. The induction strain increases with increasing volume fraction for all systems.

Note that the value of the stress on the plateaus and final steady-state stresses are independent of the starting configuration of the suspension. The initial rise in the stress at the very smallest strains does depend on the initial configuration but is not of interest here.

Figure 3 shows the variations of the stress and elastic energy for a polydispersity index of 0.1 and volume fraction of 0.8. At low shear rates, the shear stress and elastic energy reach their plateau values after a strain of about 0.1–0.3 and there is no induction strain before reaching the steady state [Figs. 3(a) and 3(b)]. At higher shear rates, there is an induction strain before a rapid drop in stress or energy before reaching steady-state values. The length of the induction strain decreases slightly with the shear rate.

The steady-state values of the shear stress and elastic energy as a function of the applied shear rate for the three polydispersity values investigated are shown in Fig. 4. Both the shear stress and elastic energy follow the Herschel-Bulkley equation. For the larger volume fractions, the onset of the plateau yield stress occurs at lower shear rates than the onset of the plateau of energy. The elastic energy of the system is apparently less sensitive than the shear stress to shear rate at low shear rates. The shear stress exhibits a discontinuity at an intermediate shear rate for the suspensions with low polydispersity and the lowest volume fraction. The discontinuity occurs when the polydispersity, volume fraction and shear rate are such that there is an induction strain with a stress plateau prior to the rapid drop to the steady-state shear stress. These conditions are indicated by open symbols in Fig. 4. The discontinuity shifts to higher shear rates with an increase in the polydispersity and volume fraction. A similar behavior of the shear stress was reported by Chen *et al.* [37] for charge-stabilized polystyrene latex particles under simple shear flow. The shear stress of a sample with a volume fraction of 0.53 showed a discontinuity as a function of the shear rate, which was interpreted as the signature of a structural transition. It is likely that rearrangements in the microstructure of the suspension under flow are also responsible for the evolution of the shear stress and elastic energy observed in Figs. 2 and 3. They are investigated in the next section.

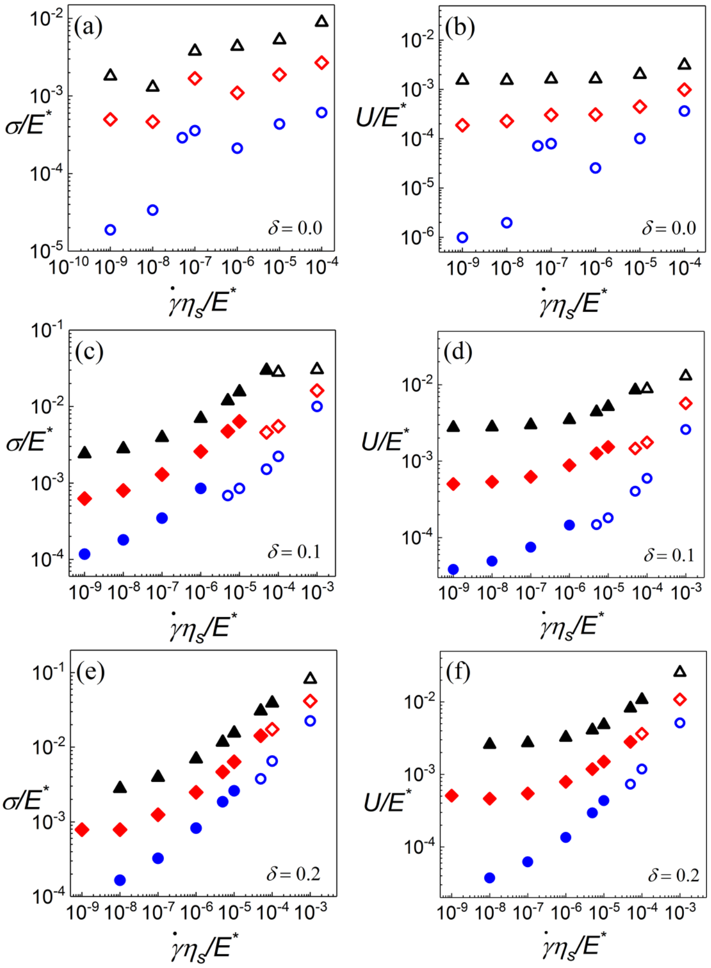

FIG. 4. Steady-state flow curve (left panels) and steady-state elastic energy (right panels) as a function of the shear rate. The following symbols are used to show results for different volume fractions: $\phi = 0.7$ (blue circle), $\phi = 0.8$ (red diamond), and $\phi = 0.9$ (black triangle). Open symbols are used to distinguish suspensions for which there is an induction strain with a stress plateau followed by a drop to steady state. Closed symbols indicate suspensions for which the stress immediately reaches the plateau.

B. Structural properties

Suspensions with a low degree of polydispersity show a different microstructure at low and high shear rates compared to the systems with a high polydispersity index. In this regard, the description of the structural properties is divided into two subsections to explore the variation with polydispersity.

1. *Microstructure of monodisperse systems*

The microstructures of jammed monodisperse suspensions and suspensions with a low degree of polydispersity ($\delta < 0.05$) are different from those of polydisperse suspensions of soft particles. To elucidate the effect of the shear deformation on the microstructure of monodisperse soft particles glasses, the pair distribution functions in the flow-gradient $g_{u\nabla}(\rho)$ and flow-vorticity $g_{u\omega}(\rho)$ planes were determined at different shear rates (where ρ is the magnitude of the two-dimensional position vector of a given particle in the flow-gradient ($u\nabla$) or flow-vorticity ($u\omega$) planes that is normalized by the radius of the particle). At both low and high shear rates, the pair distribution functions $g_{u\nabla}(\rho)$

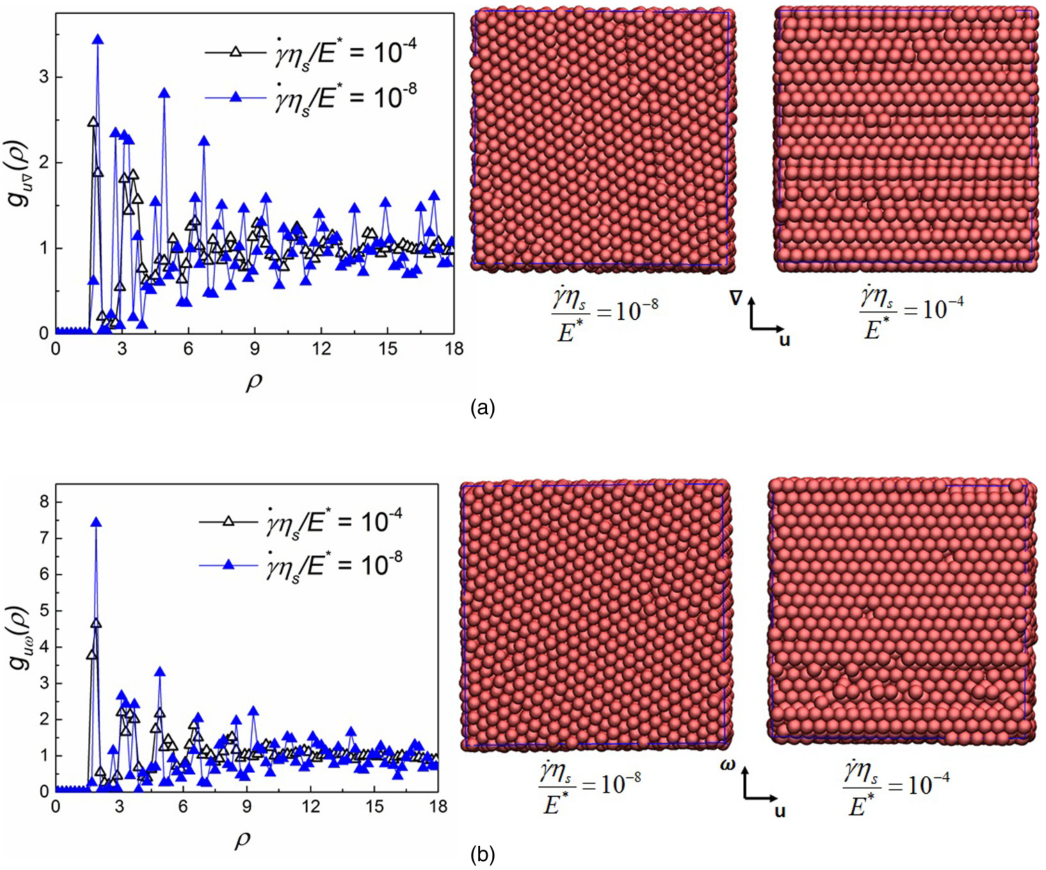

FIG. 5. (a) Flow-gradient and (b) flow-vorticity pair distribution functions of monodisperse suspension $\phi = 0.9$ as a function of the two-dimensional distance (ρ) at different shear rates.

and $g_{u\omega}(\rho)$ show several well defined peaks indicating that a crystalline structure is formed under shear deformation [see Figs. 5(a) and 5(b)]. The pair distributions in the flow-gradient plane, $g_{u\nabla}(\rho)$, at a shear rate of 10^{-8} and at a higher shear rate of 10^{-4} are different as seen in Fig. 5(a). The location of the first peaks is the same at both shear rates, but the magnitude of the peak at $\tilde{\dot{\gamma}} = 10^{-8}$ is larger than at $\tilde{\dot{\gamma}} = 10^{-4}$. This shows that at low shear rate, the number density of particles in the first neighboring shell is larger than at high shear rate. In addition the locations of the other peaks of the flow-gradient distribution functions are different, which indicates that distinct microstructures exist at low and high shear rates. The pair distribution function in the flow-vorticity plane $g_{u\omega}(\rho)$ shows a different pattern as seen in Fig. 5(b). At a high shear rate, $g_{u\omega}(\rho)$ exhibits few major and several minor peaks at small and large length scales, respectively. More distinct peaks are observed at a lower shear rate. Interestingly the peaks decay faster in the flow-vorticity plane. In addition the difference in the microstructure is clearly seen in the snapshots of the simulation box at a low and high shear rates [see Figs. 5(a) and 5(b)].

To quantify the difference in the configuration of the particles at low and high shear rates in monodisperse suspensions, the microstructures were characterized by the bond order parameters [15,62,63]. The Q_l and $\hat{W}_l$ are shown in Table I for a monodisperse suspension with $\phi = 0.9$ at shear rates of 10^{-8} and 10^{-4}. In addition the values of Q_l and $\hat{W}_l$ are also given for perfect HCP and FCC crystals. Although Q_6 and $\hat{W}_6$ values at high shear rate are slightly smaller than those of a perfect HCP, the Q_4 and $\hat{W}_4$ values are in a good agreement. Similarly, the bond order parameters values

TABLE I. Bond order parameters (Q_l and $\hat{W}_l$) for monodisperse system obtained at a volume fraction of 0.9.

System	Q_4	Q_6	$\hat{W}_4$	$\hat{W}_6$
Monodisperse, shear rate = 10^{-4}	0.1197	0.4518	0.0633	0.0001
Monodisperse, shear rate = 10^{-8}	0.1440	0.5092	−0.1404	−0.0120
HCP	0.0972	0.4848	0.1341	−0.0124
FCC	0.1909	0.5745	−0.1593	−0.0132

obtained at low shear rates match well with those of a perfect FCC lattice. We note that an increase in the shear rate changes the $\hat{W}_4$ parameter from negative to a positive, which is in agreement with the properties of FCC and HCP crystals [15]. Similar results were also observed for the suspensions with polydispersity index of 0.02. In summary, starting from an amorphous state, the shear flow rearranges the soft monodisperse particles into a FCC structure at low shear rates and a HCP lattice at high shear rate.

2. *Microstructure of polydisperse suspensions*

The flow-gradient and flow-vorticity correlation functions $g_{u\nabla}(\rho)$ and $g_{u\omega}(\rho)$ were determined at several strain values ($\gamma = 1,10,20,30,40,$ and 100) to examine the effect of the strain (or the shearing time) on the microstructure of the suspensions. Results for a volume fraction of 0.9 and polydispersity index of 0.1 are shown in Fig. 6 when the applied shear rate is $\tilde{\dot{\gamma}} = 10^{-4}$. As seen in Fig. 6(a), $g_{u\nabla}(\rho)$ initially reveals an amorphous structure, indicated by the rapid decay of the peaks over a few particle radii. The structure becomes more ordered as the strain increases beyond about 30. This ordering coincides with the rapid drop of the shear stress after the stress plateau region, which is shown in Fig. 2. The growth of the well-defined secondary peaks in the pair distribution function $g_{u\nabla}(\rho)$ indicates that layers of particles parallel to the flow-vorticity plane are being formed. The simulation box view in the flow-gradient plane [Fig. 6(a), right panel] clearly shows that at a very large strain ($\gamma = 100$), particles form layerlike structures parallel to the flow-vorticity plane. A close examination of the simulation box in the flow-vorticity plane reveals a sixfold symmetry that vanishes at long distance. The peaks of the pair distribution function in the flow-vorticity plane [Fig. 6(b)] decay more rapidly than in the flow-gradient plane [Fig. 6(a)], also indicating a less ordered structure. The same phenomenon occurs for all other systems with different volume fractions and degree of polydispersity.

It is interesting to compute the coefficient $g_{2,-2}(r/R)$ of the expansion of the pair distribution function into spherical harmonics (r corresponds to the three-dimensional distance between particles). It quantifies the angular asymmetry caused by accumulation and depletion of particles between the compression and extension axis [52]. It is shown in Fig. 7(a) for different strain values. The first minimum point of $g_{2,-2}(r/R)$ corresponds to the particle accumulation along the compression axes, and the maximum point corresponds to the depletion of the particles in the extension axis. The minimum point occurs at $r_m/R = 1.70$ for $\gamma \leqslant 30$. As the strain increases, the position of minimum shifts to larger length scales ($r_m/R = 1.75$). This observation indicates that during the structural rearrangement, particles become less compressed due to the formation of layered structures in the flow direction, which explains the decrease in elastic energy seen in Fig. 2. Furthermore, the behavior of $g_{2,-2}(r/R)$ does not change at intermediate strains $5 \leqslant \gamma \leqslant 20$, which corresponds to the stress plateau. In addition, the two-dimensional pair distribution functions at a low and high strain are shown in Fig. 7(b). At $\gamma = 5$, there are contacts in the flow and gradient directions, while the contacts in the gradient direction vanish with an increase in the strain that confirms the formation of layers parallel to the flow-vorticity plane.

The effect of the shear rate on the microstructure of the system with a volume fraction of 0.9 and polydispersity degree of 0.1 in the flow-gradient and flow-vorticity planes is shown in Figs. 8(a) and 8(b). At lower shear rates, the system is amorphous, and at higher shear rates, the structure shows

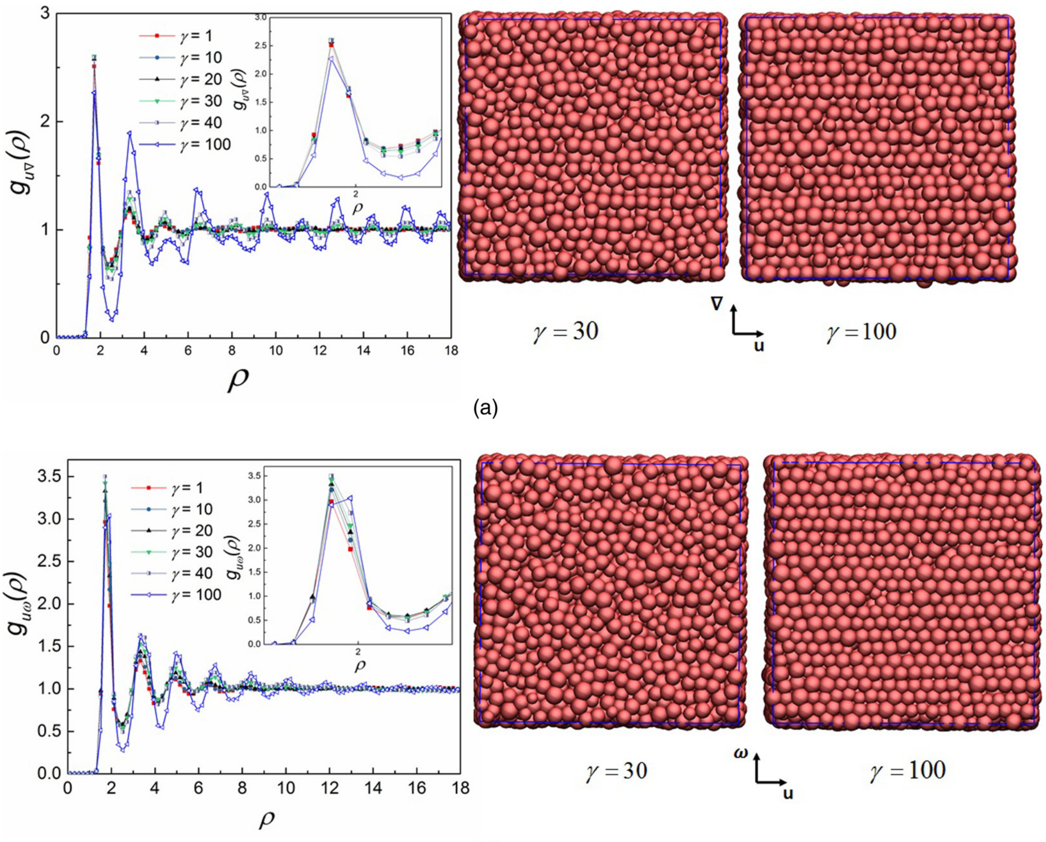

(a)

(b)

FIG. 6. (a) Pair distribution function in the flow-gradient plane (left panel) and flow-vorticity view of the simulation box during the shear flow (right panels). (b) Pair distribution function in the flow-vorticity plane (left panel) and flow-vorticity view of the simulation box during the shear flow (right panels). Results are shown for a suspension with $\delta = 0.1$, $\phi = 0.9$, and applied shear rate of $\tilde{\gamma} = 10^{-4}$.

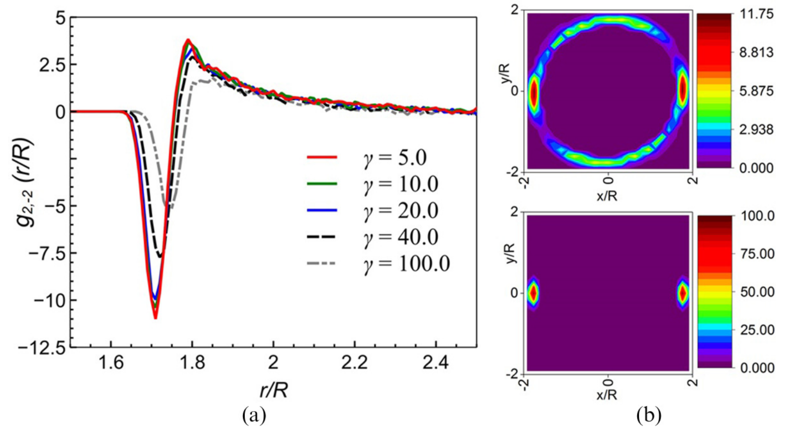

(a) (b)

FIG. 7. (a) $g_{2,-2}(r/R)$ as a function of the reduced distance for a suspension with $\delta = 0.1$, $\phi = 0.9$. (b) Two-dimensional pair distribution function at $\gamma = 5$ (top) and $\gamma = 100$ (bottom) obtained at $z = 0$. The applied shear rate is $\tilde{\gamma} = 10^{-4}$.

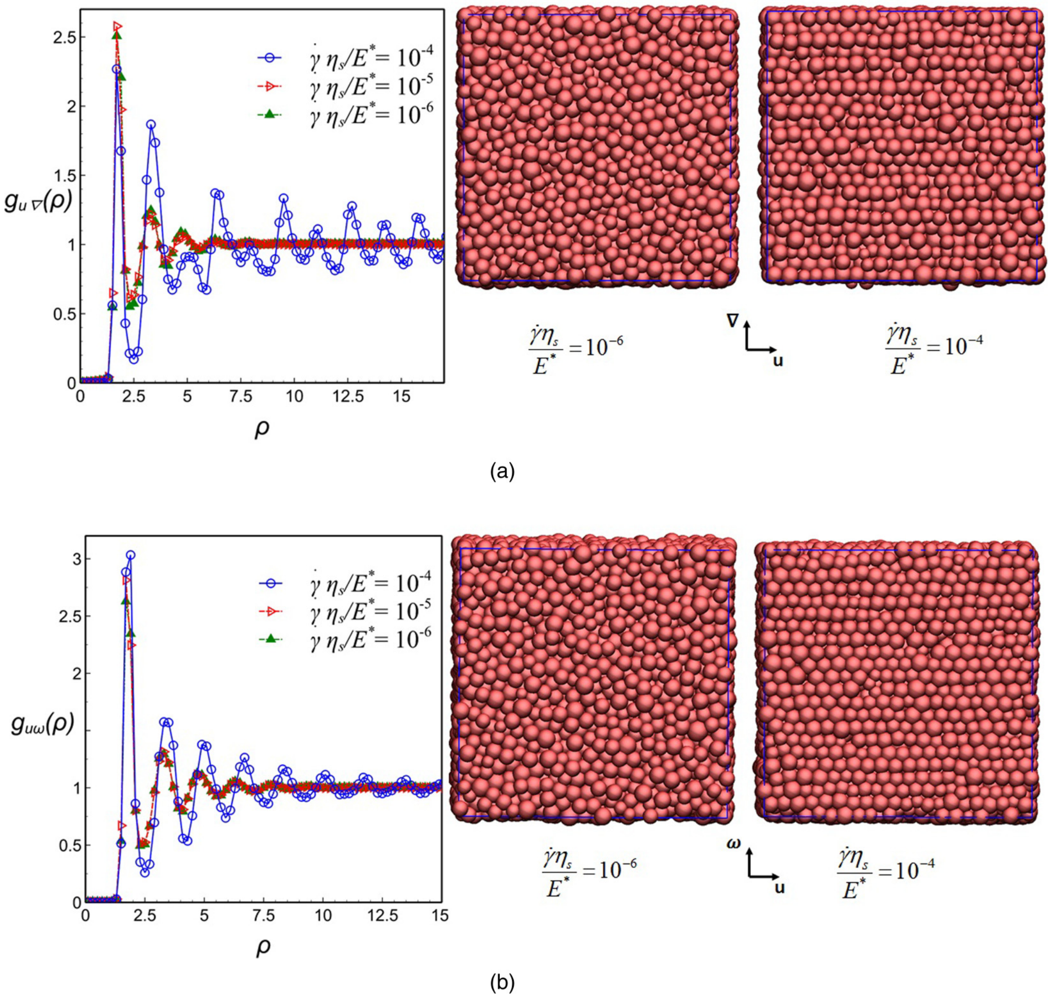

FIG. 8. (a) Effect of shear rate on the pair distribution function in the flow-gradient plane (left panel) and flow-gradient view of the end configuration of simulation box under different shear rates (right panel). (b) Effect of shear rate on the pair distribution function in the flow-vorticity plane (left panel) and flow-vorticity view of the end configuration of simulation box under different shear rates (right panel). Results are shown for the suspension with a polydispersity of 0.1 and volume fraction of 0.9.

a layerlike phase. As the shear rate increases to 10^{-4}, the flow-gradient distribution function shows distinct peaks, and the flow-vorticity distribution function indicates a weaker degree of structural rearrangement at larger length scale as already discussed above. Finally, we also varied the volume fraction and the polydispersity index. An increase in the volume fraction of the suspension at constant shear rate and polydispersity index leads to a more amorphous structure (see Fig. S1 [66]). In addition, an increase in the polydispersity index of the suspensions at a constant volume fraction and shear rate can delay the phase transition during the shear deformation (see Fig. S2 [66]).

C. DISCUSSION

1. Dynamical state diagram

Towards creating a state-space map of structure as a function of shear rate, we define a dimensionless number λ that is equal to the ratio of the shear energy to the elastic energy for a

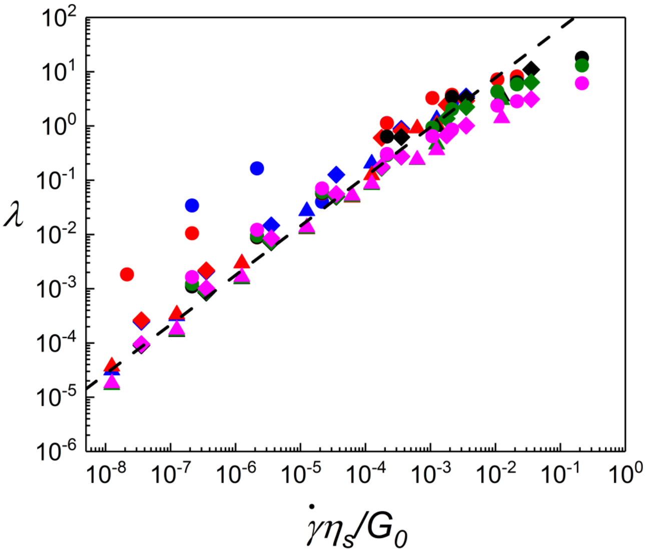

FIG. 9. Master curve of λ as a function of the reduced shear rate ($\dot{\gamma}\eta_s/G_0$). The power-law fit is shown using a dashed line. To distinguish the volume fraction of different suspensions, the following symbols are used: $\phi = 0.7$ (circle), $\phi = 0.8$ (diamond), and $\phi = 0.9$ (triangle). To distinguish the polydispersity degree of each suspension, the following coloring scheme is used: $\delta = 0$ (blue), $\delta = 0.02$ (red), $\delta = 0.05$ (black), $\delta = 0.1$ (green), and $\delta = 0.2$ (magenta).

given soft particle in the system. The shear energy per particle is defined as $U_s = \frac{4\pi R^3\dot{\gamma}\eta_s}{3\phi}$ and is calculated for all systems as a function of the shear rate. The values of the average elastic energy were determined as a function of the shear rate, and values of λ were calculated using: $\lambda = \frac{U_s}{U_{\text{sim.}}}$, where $U_{\text{sim.}}$ is the elastic energy determined in simulations, as a function of the applied shear rate. This parameter is shown as a function of the shear rate at different volume fractions for a system with a degree of polydispersity of 0.2 in Fig. S3 [66]. As seen in Fig. S3, λ increases with an increase in the shear rate in a power-law due to that fact that the elastic energy increases with $\sim\tilde{\dot{\gamma}}^a$, where $a < 1.0$. The exponents of the power-law fit are 0.6, 0.76, and 0.82 for a suspension with a polydispersity of 0.2 and volume fraction of 0.7, 0.8, and 0.9, respectively. An increase in the volume fraction of the system results in a decrease in value of λ at a given shear rate due to fact that the increase in the elastic energy is larger than the increase in the shear energy for the particles at a given shear rate when volume fraction increases. Interestingly, the transition from an amorphous to a layerlike structure occurs at $\lambda \cong 1$ for suspensions with polydispersity index larger than 0.02. This observation indicates that the shear flow is necessary to overcome the energy barrier associated with the rearrangement of the microstructure. At low shear rates, the value of the shear energy is smaller than the elastic energy and the structure is amorphous. At high shear rates, the shear energy prevails and induces planar structures in the polydispersed systems.

In Fig. S3, the parameter λ is shown to depend on several parameters which are the shear rate, volume fraction, solvent viscosity, and particle elasticity. To rationalize these variations we propose to introduce the nondimensional shear rate $\dot{\gamma}^* = \dot{\gamma}\eta_s/G_0$ by scaling the shear rate by the characteristic time η_s/G_0, where η_s is the solvent viscosity and G_0 the storage modulus of the suspension (G_0 is a function of the contact elasticity E^* and volume fraction [64]). η_s/G_0 is a microscopic time scale that expresses the competition between the elastic driving forces and the dissipative viscous forces acting on the caged particles [65]. Employing this parameter, values of λ obtained at different volume fractions and degrees of polydispersity can be collapsed onto a master curve as shown in Fig. 9. In addition, λ can be fitted to the power-law function: $\lambda = 514.1(\dot{\gamma}\eta_s/G_0)^{0.90}$. The exponent

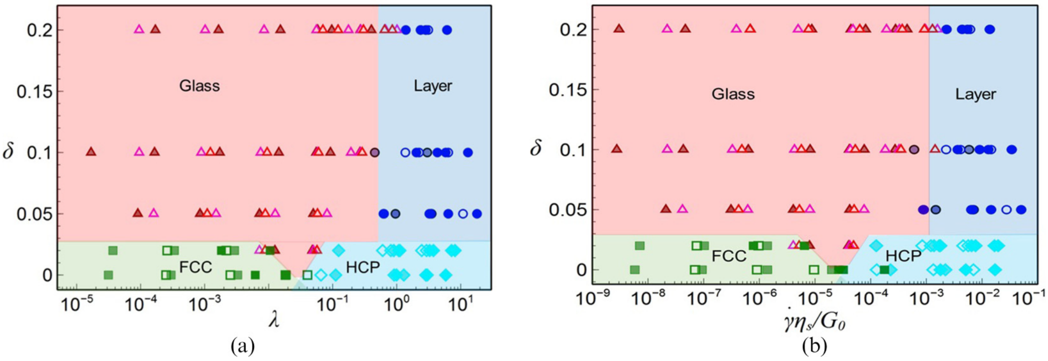

FIG. 10. State diagram of the soft particle glasses in shear flow as a function of (a) λ and (b) nondimensional shear rate (determined using the low frequency modulus G_0). Following symbols are used to show the state of each suspension:$\phi = 0.7$: layered structure (blue circle), glass (open red triangle), HCP (cyan square), and FCC (green square). $\phi = 0.8$: layered structure (open blue circle), glass (open magenta triangle), HCP (open cyan square), and FCC (open green square). $\phi = 0.9$: layered structure (half-filled blue circle), glass (half-filled brown triangle), HCP (half-filled cyan square), and FCC (half-filled green square).

of the power-law equation is 0.9, which is close to unity, indicating that $\dot{\gamma}^*$ and λ are essentially proportional up to $\lambda \cong 1$. Using this relationship (see Fig. 9), λ can be easily predicted for a given suspension in shear flow. We note that here the suspensions form FCC, HCP, glass, and layered phase in this study, but regadless of the state of a given suspension the values of λ obtained from suspensions with different volume fractions and polidyspersity indices collapse onto a master curve.

This suggests that a state diagram of the systems can be constructed using the parameter λ or $\dot{\gamma}\eta_s/G_0$ and the polydispersity, as shown in Figs. 10(a) and 10(b). The state of the suspensions as a function of the λ shows several different regions [Fig. 10(a)]. At low λ and δ, structures tend to be FCC, and an increase in λ leads to a transition to HCP. This transition occurs at $\lambda \sim 0.1$. For the suspensions with larger degrees of polydispersity ($\delta > 0.02$), no FCC structure was observed at small values of λ. Instead, they show a glassy structure. Further increase in λ leads to the formation of layerlike structures above $\lambda \sim 1.0$. Figure 10(b) shows the state diagram of soft particle glasses under shear flow as a function of the nondimensional shear rate $\dot{\gamma}\eta_s/G_0$. The resulting state diagram is very similar to that obtained using the λ parameter but the advantage of this new representation is to be able to predict the state and the behavior of a suspension from the knowledge of experimental parameters which can be easily determined. As seen in the figure, the transition from FCC to HCP structure occurs at a dimensionless shear rate of 10^{-5}, and the layered structure is formed around a reduced shear rate of 10^{-3}.

We investigated the stability of the shear induced structures upon flow cessation. When the shear rate is decreased from values where the layered structure was formed, the suspension returns to the glassy phase for the suspensions with a polydispersity degree larger than 0.02 (see Fig. S4 in Supplemental Materials [66]). Similarly, complete flow cessation returns the suspension to an original glassy state. For a suspension with a degree of polydispersity lower than 0.02, the HCP structure obtained at high shear rates transforms into an FCC structure when the shear rate is decreased. The existence if a reversible transition from HCP to FCC for suspensions with low polydispersity is well supported by the variations of the bond order parameters shown in Table SI (see Supplemental Materials [66]).

2. *Interpretation of crystallization in terms of shear activated phenomena*

The shear stress and the elastic energy of monodisperse and polydisperse suspensions show a rapid drop as a function of strain after reaching a plateau region. The analysis of the microstructure also reveals that this drop is associated with structural rearrangement in the

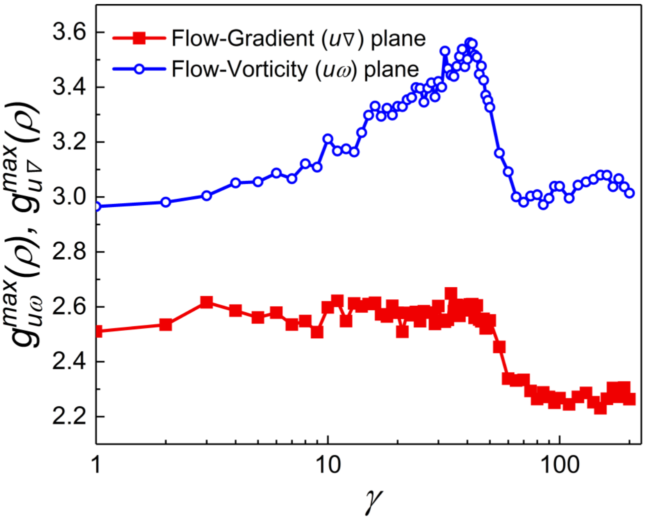

FIG. 11. The magnitude of the pair distribution functions at the first peak for a system with a volume fraction of 0.9 and polydispersity of 0.1. The applied shear rate is $\tilde{\dot{\gamma}} = 10^{-4}$.

flow-gradient and flow-vorticity planes. The existence of the plateau in the stress and elastic energy raises several important questions. Why is there an induction period during the shear flow? How does the microstructure change during this period? Is there an activated process that leads to the crystallization of the suspensions?

To address these questions, the maximum points of the two-dimensional pair distribution functions in both flow-gradient and flow-vorticity planes are plotted against the strain for a system with a volume fraction of 0.9 and polydispersity of 0.1 in Fig. 11. This maximum value corresponds to the magnitude of the pair distribution functions at the first peak, whose location does not change as a function of the strain. The pair distribution function in the flow-gradient plane, $g_{u\nabla}^{\max}(\rho)$, is constant before the drop in stress (this constant period in $g_{u\nabla}^{\max}(\rho)$ values is comparable with the induction strain as it was seen in Fig. 1), and then it too drops and reaches steady state. This rapid decrease shows that the number density of particles in the first neighbor shell decreases when the layered structure is formed compared to the glassy state. On the other hand, the maximum of the pair distribution function in the flow-vorticity plane monotonically increases as a function of the strain in the plateau region of the shear stress as a function of strain. Interestingly, we see that the reduction in the maximum value of $g_{u\omega}^{\max}(\rho)$ occurs earlier in the flow-vorticity plane compared to that in the flow-gradient plane. These observations indicate that particles initially rearrange in the flow-vorticity plane during the induction strain. During the rapid drop in the stress, layers parallel to the flow-vorticity plane are formed. At higher strains, height of the first peak in both planes reaches steady-state values. This result (not shown here) is also seen in the monodispersed systems.

The induction strain decreases with an increase in the shear rate. During the induction period, particles are forced into layers requiring them to overcome an energy barrier E. There are no thermal forces in our simulations, but the shear stress due to the elastic forces on the particles drives the dynamics. Thus, we postulate that the rate S of successful collisions that drives particles into layers follows the relation

$$S \sim \frac{\eta\dot{\gamma}}{G_0} \exp\left(-\frac{E}{\tilde{\sigma}}\right), \tag{10}$$

where $\frac{\eta_s\dot{\gamma}}{G_0}$ and $\tilde{\sigma}$ are reduced shear rate and shear stress, respectively, and E is an energy barrier scaled by E^*R^3. The induction time τ_{IND} must be inversely proportional to the rate of collision

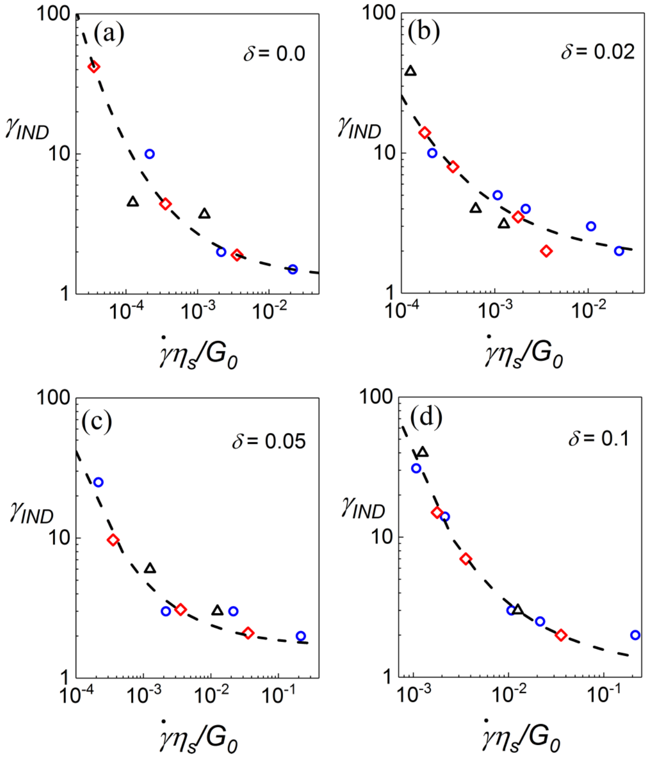

FIG. 12. Induction strain γ_{IND} as a function the reduced shear rate with respect to the low-frequency modulus G_0 for suspensions with the polydispersity degree of (a) $\delta = 0.0$, (b) $\delta = 0.02$, (c) $\delta = 0.05$, and (d) $\delta = 0.1$. The fit parameters are for $\delta = 0.0$: $A = 1.269$, $E/\sigma_y = 22.65$, $K = 917.2$, for $\delta = 0.02$: $A = 1.0$, $E/\sigma_y = 29.54$, $K = 700$; for $\delta = 0.05$:$A = 1.664$, $E/\sigma_y = 26.55$, $K = 725$; and for $\delta = 0.1$: $A = 1.097$, $E/\sigma_y = 79.42$, $K = 696.1$. To distinguish the volume fraction of different suspensions, the following symbols are used: $\phi = 0.7$ (circle), $\phi = 0.8$ (diamond), and $\phi = 0.9$ (triangle).

($\tau_{\mathrm{IND}} \sim \frac{1}{S}$). Since $\gamma_{\mathrm{IND}} \sim \tau_{\mathrm{IND}} \frac{\eta\dot{\gamma}}{G_0}$, we find $\gamma_{\mathrm{IND}} \sim \exp(\frac{E}{\tilde{\sigma}})$ for the induction strain. We can rewrite this exponential relationship by noting that the stress obeys to the Herschel-Bulkely equation: $\tilde{\sigma} = 1 + K(\eta_s\dot{\gamma}/G_0)^{1/2}$, and so

$$\gamma_{\mathrm{IND}} = A \exp\left(\frac{E/\sigma_y}{1 + K\left(\frac{\eta_s\dot{\gamma}}{G_0}\right)^{1/2}}\right). \tag{11}$$

Values of the induction strain (γ_{IND}) as a function of the reduced shear rate are shown in Fig. 12 for systems with different degrees of polydispersity and volume fractions. As seen in the figure, values of γ_{IND} for different volume fractions collapse onto a master curve for a given degree of the polydispersity. The data are successfully fitted to Eq. (11), and the corresponding fit parameters are shown in the figures for each degree of polydispersity. The values of E/σ_y are in a range of 22 to 80, which are slightly larger than the range of 10 to 20 that is obtained from the energy per particle in simulations. The K parameter shows a range of $696 < K < 918$. This range of K is larger by a factor of three compared to range of $220 < K < 320$ determined from the experimental flow curves of polyelectrolyte microgels at high shear rates [65]. As expected, the A parameter is around one. This result indicates that the structural rearrangement for sheared glassy suspensions of the monodisperse and polydisperse soft particles is an activated process. Recently, it has been argued based on 2D experiments with no flow that crystal-to-crystal transitions cannot occur without an intermediate fluid phase [67]. The results of the simulations here show that in 3D transitions from FCC to HCP do occur in one step rather than a two-step process.

IV. SUMMARY AND CONCLUDING REMARKS

In this study we investigated the effect of steady shear and polydispersity on the rheological properties and microstructure of jammed suspensions of soft particles. Our results show that soft particle glasses regardless of their volume fractions can undergo shear-induced ordering. In particular, the microstructure changes from an amorphous phase to a layerlike structure parallel to the flow-vorticity plane. This structural rearrangement is in coincidence with the reduction of the shear stress and elastic energy of the system. While the polydisperse systems show a layerlike structure, the monodisperse suspensions ($\delta = 0.0$) and the suspensions with a low degree of polydispersity ($\delta = 0.02$) behave differently. At low shear rates, the latter systems form FCC-like structure, while at higher shear rates they exhibit HCP-like lattice due to the strong effect of shear flow on the microstructure. We speculate that the state diagram for steady shear may also be applicable to oscillatory shear by replacing the shear rate by the product of the frequency and maximum strain.

Furthermore, we showed that this disorder-layering transformation is a shear activated process. There is an induction period before the layerlike structure is formed. The induction period follows a universal exponential behavior for systems with different volume fractions at a given degree of polydispersity. Our results demonstrate that the dimensionless localized energy (λ) show a universal power-law behavior as a function of the shear rate, which is normalized with respect to the low-frequency modulus of the systems. In addition, the disorder-layering transformation occurs at $\lambda \sim 1$, and a state diagram of these systems under shear flow has been constructed using this parameter. The results of this study indicate that the shear flow changes the energy landscape to allow the suspension to explore other energy states.

The results of this study provide detailed information on the relation between the microstructure and macroscopic properties of jammed suspensions. The provided state diagrams can explain the very different experimental observation on the microstructure of colloidal suspensions [20–27,29] and point to polydispersity index as an important parameter that controls the states of a suspension.

ACKNOWLEDGMENT

F.K. and R.T.B. gratefully acknowledge partial support from NSF Grant No. CBET 1336852.

[1] P. N. Pusey and W. Van Megen, Phase behaviour of concentrated suspensions of nearly hard colloidal spheres, Nature **320**, 340 (1986).

[2] P. N. Pusey, Colloidal glasses, J. Phys.: Condens. Matter **20**, 494202 (2008).

[3] J. L. Barrat and J. P. Hansen, On the stability of polydisperse colloidal crystals, J. Phys. (Paris) **47**, 1547 (1986).

[4] P. G. Bolhuis and D. A. Kofke, Monte Carlo study of freezing of polydisperse hard spheres, Phys. Rev. E **54**, 634 (1996).

[5] D. A. Kofke and P. G. Bolhuis, Freezing of polydisperse hard spheres, Phys. Rev. E **59**, 618 (1999).

[6] P. N. Pusey, The effect of polydispersity on the crystallization of hard spherical colloids, J. Phys. (Paris) **48**, 709 (1987).

[7] S.-E. Phan, W. B. Russel, J. Zhu, and P. M. Chaikin, Effects of polydispersity on hard sphere crystals, J. Chem. Phys. **108**, 9789 (1998).

[8] H. Senff and W. Richtering, Temperature sensitive microgel suspensions: Colloidal phase behavior and rheology of soft spheres, J. Chem. Phys. **111**, 1705 (1999).

[9] S. E. Paulin, B. J. Ackerson, and M. S. Wolfe, Equilibrium and shear induced nonequilibrium phase behavior of PMMA microgel spheres, J. Colloid Interface Sci. **178**, 251 (1996).

[10] J. J. Crassous, M. Siebenbürger, M. Ballauff, M. Drechsler, O. Henrich, and M. Fuchs, Thermosensitive core-shell particles as model systems for studying the flow behavior of concentrated colloidal dispersions, J. Chem. Phys. **125**, 204906 (2006).

[11] D. Paloli, P. S. Mohanty, J. J. Crassous, E. Zaccarelli, and P. Schurtenberger, Fluid-solid transitions in soft-repulsive colloids, Soft Matter **9**, 3000 (2013).

[12] B. Sierra-Martin and A. Fernandez-Nieves, Phase and non-equilibrium behaviour of microgel suspensions as a function of particle stiffness, Soft Matter **8**, 4141 (2012).

[13] G. A. Mcconnell, A. P. Gast, J. S. Huang, and S. D. Smith, Disorder-Order Transitions in Soft Sphere Polymer Micelles, Phys. Rev. Lett. **71**, 2102 (1993).

[14] D. Vlassopoulos and M. Cloitre, Tunable rheology of dense soft deformable colloids, Curr. Opin. Colloid Interface Sci. **19**, 561 (2014).

[15] P. J. Steinhardt, D. R. Nelson, and M. Ronchetti, Bond-orientational order in liquids and glasses, Phys. Rev. B **28**, 784 (1983).

[16] D. Vlassopoulos and G. Fytas, in *High Solid Dispersions*, edited by M. Cloitre (Springer, Berlin/Heidelberg, 2010), pp. 1.

[17] R. T. Bonnecaze and M. Cloitre, in *High Solid Dispersions*, edited by M. Cloitre (Springer, Berlin/Heidelberg, 2010), pp. 117.

[18] C. Pellet and M. Cloitre, The glass and jamming transitions of soft polyelectrolyte microgel suspensions, Soft Matter **12**, 3710 (2016).

[19] J. Vermant and M. J. Solomon, Flow-induced structure in colloidal suspensions, J. Phys.: Condens. Matter **17**, R187 (2005).

[20] R. L. Hoffman, Discontinuous and dilatant viscosity behavior in concentrated suspensions. I. Observation of a flow instability, Trans. Soc. Rheol. **16**, 155 (1972).

[21] B. J. Ackerson, Shear induced order and shear processing of model hard sphere suspensions, J. Rheol. **34**, 553 (1990).

[22] B. J. Ackerson and P. N. Pusey, Shear-Induced Order in Suspensions of Hard Spheres, Phys. Rev. Lett. **61**, 1033 (1988).

[23] J. Liu, D. A. Weitz, and B. J. Ackerson, Coherent crystallography of shear-aligned crystals of hard-sphere colloids, Phys. Rev. E **48**, 1106 (1993).

[24] M. D. Haw, W. C. K. Poon, and P. N. Pusey, Direct observation of oscillatory-shear-induced order in colloidal suspensions, Phys. Rev. E **57**, 6859 (1998).

[25] J. Vermant, L. Raynaud, J. Mewis, B. Ernst, and G. G. Fuller, Large-scale bundle ordering in sterically stabilized latices, J. Colloid Interface Sci. **211**, 221 (1999).

[26] P. Panine, T. Narayanan, J. Vermant, and J. Mewis, Structure and rheology during shear-induced crystallization of a latex suspension, Phys. Rev. E **66**, 022401 (2002).

[27] Y. L. Wu, D. Derks, A. Van Blaaderen, and A. Imhof, Melting and crystallization of colloidal hard-sphere suspensions under shear, Proc. Natl. Acad. Sci. USA **106**, 10564 (2009).

[28] N. Koumakis, J. F. Brady, and G. Petekidis, Amorphous and ordered states of concentrated hard spheres under oscillatory shear, J. Non-Newtonian Fluid Mech. **233**, 119 (2016).

[29] T. H. Besseling, M. Hermes, A. Fortini, M. Dijkstra, A. Imhof, and A. Van Blaaderen, Oscillatory shear-induced 3D crystalline order in colloidal hard-sphere fluids, Soft Matter **8**, 6931 (2012).

[30] N. Koumakis, A. B. Schofield, and G. Petekidis, Effects of shear induced crystallization on the rheology and ageing of hard sphere glasses, Soft Matter **4**, 2008 (2008).

[31] S. Butler and P. Harrowell, Shear induced ordering in simulations of colloidal suspensions: Oscillatory shear and computational artefacts, J. Chem. Phys. **105**, 605 (1996).

[32] B. J. Ackerson and N. A. Clark, Shear-Induced Melting, Phys. Rev. Lett. **46**, 123 (1981).

[33] M. Tomita and T. G. M. Van De Ven, The structure of sheared ordered latices, J. Colloid Interface Sci. **99**, 374 (1984).

[34] L. B. Chen, C. F. Zukoski, B. J. Ackerson, H. J. M. Hanley, G. C. Straty, J. Barker, and C. J. Glinka, Structural Changes and Orientational Order in a Sheared Colloidal Suspension, Phys. Rev. Lett. **69**, 688 (1992).

[35] H. M. Laun, R. Bung, S. Hess, W. Loose, O. Hess, K. Hahn, E. Hädicke, R. Hingmann, F. Schmidt, and P. Lindner, Rheological and small angle neutron scattering investigation of shear induced particle structures of concentrated polymer dispersions submitted to plane Poiseuille and Couette flowa, J. Rheol. **36**, 743 (1992).

[36] A. Imhof, A. Van Blaaderen, and J. K. G. Dhont, Shear melting of colloidal crystals of charged spheres studied with rheology and polarizing microscopy, Langmuir **10**, 3477 (1994).

[37] L. B. Chen, M. K. Chow, B. J. Ackerson, and C. F. Zukoski, Rheological and microstructural transitions in colloidal crystals, Langmuir **10**, 2817 (1994).

[38] Y. D. Yan, J. K. G. Dhont, C. Smits, and H. N. W. Lekkerkerker, Oscillatory-shear-induced order in nonaqueous dispersions of charged colloidal spheres, Phys. A **202**, 68 (1994).

[39] C. Dux, S. Musa, V. Reus, H. Versmold, D. Schwahn, and P. Lindner, Small angle neutron scattering experiments from colloidal dispersions at rest and under sheared conditions, J. Chem. Phys. **109**, 2556 (1998).

[40] H. Versmold, S. Musa, and A. Bierbaum, Concentrated colloidal dispersions: On the relation of rheology with small angle x-ray and neutron scattering, J. Chem. Phys. **116**, 2658 (2002).

[41] P. Holmqvist, M. P. Lettinga, J. Buitenhuis, and J. K. G. Dhont, Crystallization kinetics of colloidal spheres under stationary shear flow, Langmuir **21**, 10976 (2005).

[42] L. B. Chen, B. J. Ackerson, and C. F. Zukoski, Rheological consequences of microstructural transitions in colloidal crystals, J. Rheol. **38**, 193 (1994).

[43] Y. D. Yan and J. K. G. Dhont, Shear-induced structure distortion in nonaqueous dispersions of charged colloidal spheres via light scattering, Phys. A (Amsterdam, Neth.) **198**, 78 (1993).

[44] K. Mortensen, W. Brown, and B. Nordén, Inverse Melting Transition and Evidence of Three-Dimensional Cubatic Structure in a Block-Copolymer Micellar System, Phys. Rev. Lett. **68**, 2340 (1992).

[45] E. Stiakakis, A. Wilk, J. Kohlbrecher, D. Vlassopoulos, and G. Petekidis, Slow dynamics, aging, and crystallization of multiarm star glasses, Phys. Rev. E **81**, 020402 (2010).

[46] D. Vlassopoulos (private communication).

[47] S. Markus, L. Peter, and R. Walter, Structure formation in thermoresponsive microgel suspensions under shear flow, J. Phys.: Condens. Matter **16**, S3861 (2004).

[48] J. F. Berret, F. Molino, G. Porte, O. Diat, and P. Lindner, The shear-induced transition between oriented textures and layer-sliding-mediated flows in a micellar cubic crystal, J. Phys.: Condens. Matter **8**, 9513 (1996).

[49] J. Jiang, C. Burger, C. Li, J. Li, M. Y. Lin, R. H. Colby, M. H. Rafailovich, and J. C. Sokolov, Shear-induced layered structure of polymeric micelles by SANS, Macromolecules **40**, 4016 (2007).

[50] C. R. López-Barrón, N. J. Wagner, and L. Porcar, Layering, melting, and recrystallization of a close-packed micellar crystal under steady and large-amplitude oscillatory shear flows, J. Rheol. **59**, 793 (2015).

[51] A. Nikoubashman, G. Kahl, and C. N. Likos, Flow quantization and nonequilibrium nucleation of soft crystals, Soft Matter **8**, 4121 (2012).

[52] J. R. Seth, L. Mohan, C. Locatelli-Champagne, M. Cloitre, and R. T. Bonnecaze, A micromechanical model to predict the flow of soft particle glasses, Nat. Mater. **10**, 838 (2011).

[53] L. Mohan, C. Pellet, M. Cloitre, and R. Bonnecaze, Local mobility and microstructure in periodically sheared soft particle glasses and their connection to macroscopic rheology, J. Rheol. **57**, 1023 (2013).

[54] M.-D. Lacasse, G. S. Grest, D. Levine, T. G. Mason, and D. A. Weitz, Model for the Elasticity of Compressed Emulsions, Phys. Rev. Lett. **76**, 3448 (1996).

[55] B. D. Lubachevsky and F. H. Stillinger, Geometric properties of random disk packings, J. Stat. Phys. **60**, 561 (1990).

[56] J. R. Seth, M. Cloitre, and R. T. Bonnecaze, Influence of short-range forces on wall-slip in microgel pastes, J. Rheol. **52**, 1241 (2008).

[57] K. K. Liu, D. R. Williams, and B. J. Briscoe, The large deformation of a single micro-elastomeric sphere, J. Phys. D: Appl. Phys. **31**, 294 (1998).

[58] A. W. Lees and S. F. Edwards, The computer study of transport processes under extreme conditions, J. Phys. C: Solid State Phys. **5**, 1921 (1972).

[59] S. Plimpton, Fast parallel algorithms for short-range molecular dynamics, J. Comput. Phys. **117**, 1 (1995).

[60] R. G. Larson, *The Structure and Rheology of Complex Fluids* (Oxford University Press, New York, 1999).

[61] H. J. M. Hanley, J. C. Rainwater, and S. Hess, Shear-induced angular dependence of the liquid pair correlation function, Phys. Rev. A **36**, 1795 (1987).

[62] Y. Wang, S. Teitel, and C. Dellago, Melting of icosahedral gold nanoclusters from molecular dynamics simulations, J. Chem. Phys. **122**, 214722 (2005).

[63] N. Duff and D. J. Lacks, Shear-induced crystallization in jammed systems, Phys. Rev. E **75**, 031501 (2007).

[64] J. R. Seth, M. Cloitre, and R. T. Bonnecaze, Elastic properties of soft particle pastes, J. Rheol. **50**, 353 (2006).

[65] M. Cloitre, R. Borrega, F. Monti, and L. Leibler, Glassy Dynamics and Flow Properties of Soft Colloidal Pastes, Phys. Rev. Lett. **90**, 068303 (2003).

[66] See Supplemental Material at http://link.aps.org/supplemental/10.1103/PhysRevFluids.2.093301 for the effect of volume fraction and polydispersity on the microstructure of soft particles glasses, volume fraction dependence of the nondimensional energy (λ), and bond order parameter of re-sheared monodispersed suspensions.

[67] Y. Peng, F. Wang, Z. Wang, A. M. Alsayed, Z. Zhang, A. G. Yodh, and Y. Han, Two-step nucleation mechanism in solid–solid phase transitions, Nat. Mater. **14**, 101 (2015).